Minimum Acceptance Criteria for Subsurface Scenario-based Uncertainty Models from Single Image Generative Adversarial Networks (SinGAN)

Lei Liu
leiliu@utexas.edu
University of Texas at Austin
Jose J. Salazar
Escuela Superior Politécnica del Litoral
Honggeun Jo
Inha University
Maša Prodanović
University of Texas at Austin
Michael J. Pyrcz
University of Texas at Austin

Research Article

Keywords: minimum acceptance criteria, SinGAN, subsurface uncertainty models, channelized subsurface reservoirs

Posted Date: March 15th, 2024

DOI: https://doi.org/10.21203/rs.3.rs-4101619/v1

Additional Declarations: The authors declare no competing interests.

Minimum Acceptance Criteria for Subsurface Scenario-based Uncertainty Models from Single Image Generative Adversarial Networks (SinGAN)

Lei Liu[a], Jose J. Salazar[b], Honggeun Jo[c], Maša Prodanović[a], and Michael J. Pyrcz[a,d]

[a]Hildebrand Department of Petroleum and Geosystems Engineering, The University of Texas at Austin, Austin, Texas, USA

[b]Facultad de Ingeniería en Ciencias de la Tierra, Escuela Superior Politécnica del Litoral, ESPOL, Campus Gustavo Galindo Km. 30.5 Vía Perimetral, P.O. Box 09-01-5863, Guayaquil, Ecuador

[c]Energy Resources Engineering, Inha University, Incheon, Korea

[d]Department of Geological Sciences, The University of Texas at Austin, Austin, Texas, USA

Abstract

Evaluating and checking subsurface models is essential before their use to support optimum subsurface development decision making. Conventional geostatistical modeling workflows (e.g., two-point variogram-based geostatistics and multiple-point statistics) may fail to reproduce complex realistic geological patterns (e.g., channels), or be constrained by the limited training images and computational cost. Deep learning, specifically generative adversarial network (GAN), has been applied for subsurface modeling due to its ability to reproduce spatial and geological patterns, but may fail to reproduce commonly observed nonstationary subsurface patterns and often rely on many training images with the inability to explore realizations around specific geological scenarios. We propose an enhanced model checking workflow demonstrated by evaluating the performance of single image GAN (SinGAN)-based 2D image realizations for the case of channelized subsurface reservoirs to support robust uncertainty around geological scenarios. The SinGAN is able to generate nonstationary realizations from a single training image.

Our minimum acceptance criteria expand on the work of Leuangthong, Boisvert, and others tailored to the nonstationary, single training image approach of SinGAN by evaluating the facies proportion, spatial continuity, and multiple-point statistics through histogram, semivariogram, and n-point histogram, along with evaluating the nonstationarity reproduction through multiple distribution checks ranging from local scale pixel distribution to multiscale local distribution. Additionally, our workflow incorporates reduced-dimensionality analysis through self-attention, providing a flexible approach for deep learning-based enhanced model realization to single training image comparison. With our proposed workflows, the robust application of SinGAN is possible to explore uncertainty around geological scenarios.

Keywords: minimum acceptance criteria; SinGAN; subsurface uncertainty models; channelized subsurface reservoirs

1. Introduction

Subsurface modeling and forecasting are essential components for optimum decision-making for hydrocarbon exploration and field development [1], hydrogeological resources exploration and efficient management [2, 3], optimal injection and production well locations [4], and safe and reliable CO_2 injection and long-term sequestration [5]. For all of these field scale models, the common simulated spatial feature is discrete facies (or rock type), as it represents the vast majority of variance in spatial features like porosity and permeability that impact fluid flow [6, 7]. Over smaller scales, e.g., individual rock pores, we are interested in directly reconstructing the pore spaces' geometry [8, 9]. Regardless of the modeling scale, honoring the univariate and multivariate distributions, spatial continuity and discrete geometries, and spatial nonstationarity in all of these, if present, is paramount to supporting subsurface decision-making.

A common approach for calculating facies spatial realizations is variogram-based geostatistics, including indicator-based or truncated Gaussian simulation methods, based on random function models and an established theoretical foundation [10–12]. In many cases, these variogram-based methods are sufficient to characterize and model spatial continuity that impacts subsurface fluid flow [5]. Nevertheless, these two-point variogram-based methods may fail to reproduce complex, non-linear, long-range, and categorical ordering patterns like those commonly observed in the subsurface, e.g., depositional lobes and meandering channels [4, 13].

[14] propose multiple-point statistic (MPS) simulation to address these limitations of two-point variogram-based methods. MPS utilizes a training image (TI) to infer empirical spatial multi-point distributions, i.e., beyond two points, explicitly replacing an analytical random function model via sampling the training image and reproducing multi-point statistics representing complicated spatial and geological patterns. MPS techniques can be classified into pixel-based, patch-based, and optimization-based [15]. For each, multiple point events are represented by a n-point template, N($\mathbf{u}$), centered at a location, $\mathbf{u}$, with specific categorical facies at each location, $z(\mathbf{u}_\alpha)$, $\alpha = 1, \ldots, n$. A pixel-based MPS method simulates all locations in the model grid sequentially through Monte Carlo simulation from the n-point conditional distribution sampled from the TI [16]. Patch-based methods center a template over locations to recover patterns, simulating jointly over multiple locations in the process and usually requiring additional steps such as pattern

classification and mismatch measures to minimize the mismatch between adjacent patches [17]. Pixel- and patch-based methods are sequential techniques that follow an established random path to perform the simulation. On the other hand, optimization-based algorithms are non-sequential because they seed initial simulated facies at all grids, often with a random state that honors the marginal facies distribution. Then, the algorithms minimize a loss function (including a loss component) based on the mismatch with multiple-point statistics, typically conditional probabilities of multiple-point events sampled from a training image [15].

There are two advantages of optimization-based techniques. First, the techniques exhibit equivalent proficiency when handling nonstationarity as their sequential counterparts [13, 18]. Second, optimization-based techniques are often more flexible [19] and may be more computationally- and memory-efficient than sequential techniques, thereby facilitating the simulation of more challenging and complex applications with greater ease [20]. For example, [21] develop a conditional image quilting method, which combines smaller image patches by eliminating visible seams for large 3D models, reducing computational time by at least a factor of 50. Their approach achieves similar reproduction of continuous and categorical features for hydrogeological applications, greatly improving efficiency.

Deep learning approaches have been applied for optimization-based MPS, for example, neural networks calculate realizations (also called fake images or generated images in deep learning) from a trained model to output local conditional probabilities [22, 23]. Additionally, a recursive convolutional neural network calculates MPS realizations assuming stationarity by predicting the multiple-point conditional distributions of each node in the feature maps [15].

Unlike the neural networks for the optimization-based MPS, the generative adversarial networks (GAN) are based on adversarial training of the generator and the discriminator, in other words the objective function based on the discriminator is learned [24]. GANs have been widely explored for subsurface applications, e.g., the stochastic reconstruction of porous media [25], seismic wave discrimination for earthquake warning [26], and reservoir modeling [27–30]. These initial endeavors showcase the proficiency of GANs in characterizing and reproducing spatial relationships. However, GANs necessitate numerous training images as training data to replicate the high-order statistics of interest, thereby hindering their implementation due to time-consuming data collection, extended training time, and increased memory requirements. The single-image GAN (SinGAN) addresses these GANs limitations and demonstrates its ability to generate random samples by training with a single image while reproducing nonstationarity from the training image [31].

Prior to their implementation for supporting subsurface development decision-making, the evaluation and checking of subsurface models is crucial. The works mentioned above lean towards application-oriented objectives and lack an enhanced assessment of the reproduction of nonstationary structures. Furthermore, there is a notable absence of analyses that evaluate the quality of realizations concerning features critical to the study's objective [4]. Consequently, [32] propose the minimum acceptance criteria to evaluate the quality of geostatistical models and the reproduction of inputs, including data values, property distribution of interest, and spatial continuity. Additionally, high-order checks for spatial continuity beyond the variogram are augmented to account for multiple-point statistics [7, 33].

We propose an enhanced model checking workflow tailored to evaluate the performance of SinGAN-based 2D image realizations for the case of channelized subsurface reservoirs to support robust uncertainty around geological scenarios. We evaluate the quality of realizations, reproduction of stationary and nonstationarity patterns using the following metrics: semivariograms and histograms, n-point histograms, pixel scale local distribution maps and facies proportion trend map, multiscale local distribution maps, and model dimensionality reduction analysis via self-attention. Hence, our proposed workflow enables a comprehensive and rigorous model checking of SinGAN for subsurface modeling, considering the reproduction performance of ensembles of realizations in the face of both stationarity and nonstationarity. Our proposed method may be applied for a wide range of geological scenarios and is demonstrated for four distinct patterns, including cyclicity, stationarity, medium nonstationarity (weak spatial trend), and strong nonstationarity (strong spatial trend).

The background section details more GAN applications for facies modeling and their limitations, along with a summary of the SinGAN architecture. The methodology section describes the above metrics to check the enhanced minimum acceptance criteria of the SinGAN-based realizations, followed by examples of 2D simulations and the thorough analysis of the realizations in the results and discussion section. Finally, the conclusions section highlights enhanced model checking and recommendations for future work, such as uncertainty modeling with our proposed workflow.

2. Background

Essential prerequisite details of GAN for facies modeling are followed by an explanation of the SinGAN approach.

2.1 GAN for facies modeling

Multiple developments use GAN methods for facies modeling that require numerous training images. For example, [18] use a GAN to calculate nonstationary facies spatial models along with the forward seismic model, p-wave propagation velocity. Their unconditional GAN simulation relies on multiple TIs extracted as 2D slices from a single TI. Additionally, their facies model checking includes facies histograms and semivariograms in the x and y directions.

[6] train a Bayesian GAN (BGAN) with training data derived from SNESIM MPS [34]. They consider two scenarios corresponding to conceptual models, fluvial channels [16, 35] and carbonate mounds [10]. Unlike traditional GANs, BGANs incorporate a probabilistic framework by incorporating Bayesian principles, allowing for the estimation of probability distributions per parameter learned from the training data. However, the uncertainty assessment of the model comes at the cost of increased computational time due to the need to approximate posterior distributions of the generator by stochastic sampling, resulting in more training time than a traditional GAN. Their work considers three quality check metrics, histograms and semivariograms of facies, and structural similarity index (SSIM) for comparing luminance, contrast, and structures between TI and generated realizations.

[36] reconstruct geological models by combining GAN, PatchGAN discriminator, and a U-Net architecture. They capture the spatial and geological patterns using 2D sections from the 3D volume as conditioning data and check the quality of their

results using facies histograms and semivariograms. Similarly, [27] train a conditional GAN with realizations conditioned to hard data, conditioned with numerical codes representing geological properties, that impose geological characteristics of a river, like orientation and type (e.g., meandering and braided). [37] propose shift-invariant convolutional layers in the PatchGAN model to avoid inconsistency and artifacts in generated subsurface geological models.

Unlike previous GANs that require a large number of TIs, multiple attempts exist to use a single TI for GAN training. For example, [38] develop the spatial GAN (SGAN) that uses a single TI to generate unconditional realizations. Their work experiments on the stationary channelized training image from [39]. The quality assessment examines the two-point probability function, connectivity function, and average facies proportions. [30] introduce multiple-stage concurrent GAN (MSCGAN) consisting of multiple GANs with various coarse- and fine-scale stages, allowing the model to transfer parameter information between stages. MSCGAN uses one TI to reconstruct fluvial reservoirs. Their work evaluates the performance of MSCGAN on a stationary channel case, omitting consideration of other types of channelized reservoirs (e.g., nonstationarity). Furthermore, their model check is based on comparing the performance of SinGAN and MSCGAN.

2.2 SinGAN

The SinGAN architecture is a hierarchical, or pyramidal, set of GANs that trains with a single image, but sequentially produces multiple random images, each at different scales, while retaining the original image patch distributions, i.e., nonstationarity in the training image [31]. This pyramid architecture sequentially includes a paired generator and a discriminator network for each scale, and the training proceeds from the coarsest scale to the finest scale. At the coarsest scale, the generator takes the random noise input and generates the realization sample. As the training progresses to finer scales, the generator trains the random noise and an upsampling of the image generated from the previous scale, effectively filling in an increasing amount of detail. The discriminator at each scale discriminates the true down-sampled image and the generated realization from the generator.

The SinGAN architecture for our case of channelized reservoir modeling is shown in Figure 1. In what follows, the generators are noted as $\{G_0, \ldots, G_{N-1}, G_N\}$, the discriminators are $\{D_0, \ldots, D_{N-1}, D_N\}$. The real images are $\{y_0, \ldots, y_{N-1}, y_N\}$ and y_n is a downsampling version of y by a factor of r^n. The random noise is noted by $\{z_0, \ldots, z_{N-1}, z_N\}$, and the generated realizations are $\{x_0, \ldots, x_{N-1}, x_N\}$.

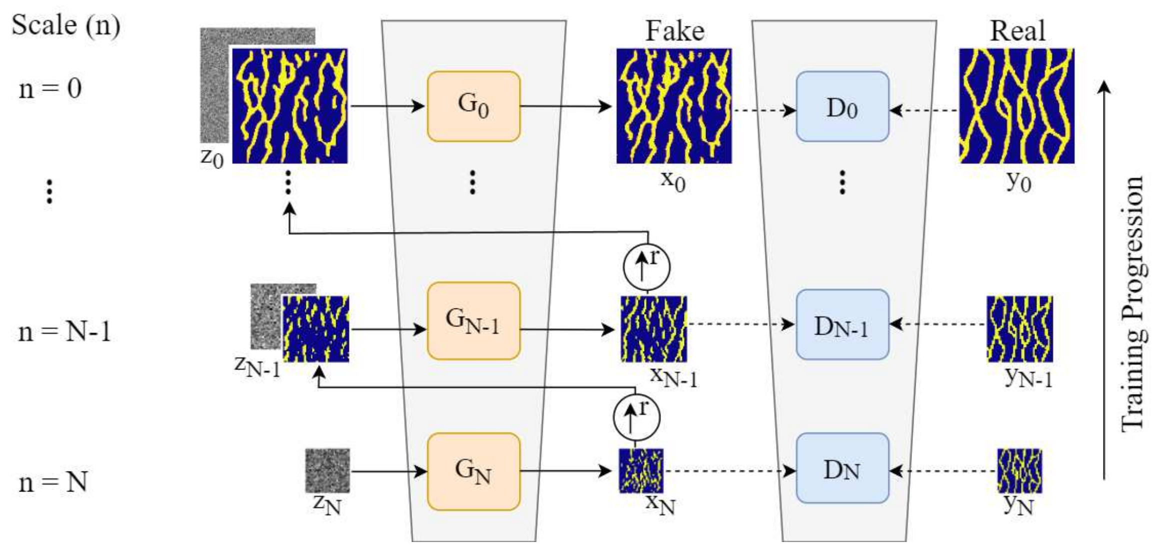

Figure 1. The SinGAN architecture for channel model generation (adapted from [31]). The model consists of a pyramid of GANs, and the training is conducted in a coarse-to-fine manner. The first,

coarsest generator (G_N) learns coarse features and adds more details as the training goes up the pyramid from course to fine scales (n goes from N to 0). The random noise at each scale follows standard Gaussian distribution.

At the coarsest scale (N), the generator (G_N) receives a random noise (z_N), and generates a coarse image sample (x_N) at the coarsest scale (Equation 1). For the remaining scales ($n < N$), the generator ($G_{N-1}, \ldots, G_0$) injects the upsampled generated image from the previous scale ($(x_{n+1}) \uparrow^r$) along with a random noise ($z_{N-1}, \ldots, z_0$), and generates a realization sample with the same resolution at the corresponding scale ($x_{N-1}, \ldots, x_0$) (Equation 2).

$$x_N = G_N(z_N) \tag{1}$$

$$x_n = (x_{n+1}) \uparrow^r + G_n(z_n, (x_{n+1}) \uparrow^r), n < N \tag{2}$$

$$\text{loss} = \min_{G_n} \max_{D_n} L_{adv}(G_n, D_n) + \alpha L_{rec}(G_n) \tag{3}$$

$$L_{rec} = \text{RMSE}(x_n, y_n) \tag{4}$$

The discriminator (D) distinguishes the real training image (y) and the generated image (x) at each scale. The generators (G) have the same architectural design, as shown in Figure 2. Moreover, Figure 2 shows that the upsampled image from the old scale ($(x_{n+1}) \uparrow^r$) is passed sequentially through five convolutional layers (labeled as Conv) along with a random noise (z_n). The output after convolutional layers is then added to the upsampled image, leading to the final output of G_n, which is x_n. The discriminators also share a network design similar to the generators but reversed, deconvolution with the same number of layers, 5, hence, having the same receptive field and learning the image structures with a decreasing effective patch size as the training progresses to the fine scale. The loss function (loss) during the training process follows the SinGAN training (Equation 3, 4), which consists of an adversarial loss (L_{adv}), penalizing the distribution of the generated sample and the training image, and a reconstruction loss (L_{rec}), determining the standard deviation of the noise, and a hyperparameter α, balancing the adversarial loss and the reconstruction loss [31]. The adversarial loss uses the WGAN-GP loss [40] and the final discrimination score after 5 layers is the average over the patch discrimination map. The reconstruction loss is the root mean squared error (RMSE) between the generated sample and the real image.

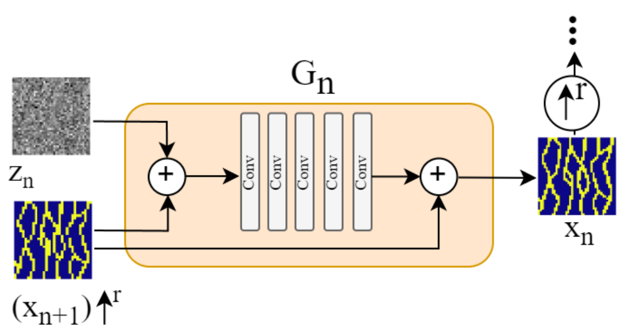

Figure 2. Generator ($G_0, \ldots, G_{N-1}$ in Figure 1) architecture in SinGAN (adapted from [31]). The generator receives a random noise and an upsampling realization from the previous scale. These inputs are processed through 5 convolutional layers, and then the output is added to the upsampling realization leading to the final output.

3. Methodology

We develop enhanced validation metrics based on the minimum acceptance criteria to support robust uncertainty around different subsurface geological scenarios [6, 18, 29, 30, 32, 36, 41, 42]. The detailed discussions on these metrics are included below.

Variograms check the spatial continuity reproduction [43, 44]. We calculate the indicator semivariogram of the training images in the major and minor directions of spatial continuity and compare them with the generated realizations by quantifying with descriptive statistics, P25 and P75. Histograms check the reproduction of channel proportions. We calculate the channel proportions histogram over multiple realizations and compare them with the training image proportion with statistical quantification, P25, mean, and P75.

N-point histograms check the higher-order statistics of generated realizations by applying multiple-point statistics (MPS) [4, 33, 45]. Here, we apply the n-point density function from [45] to compare the conditional probabilities multi-point patterns. For example, the 5-point configuration has 30 possible configurations for the case that both channel and mud exist, as shown in Figure 3.

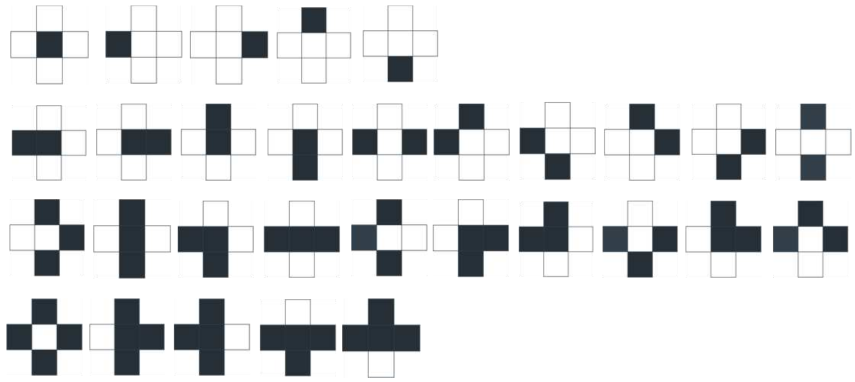

Figure 3. All MPS patterns for a 5-point configuration. The black grid refers to the channel, and the white grid refers to mud. The first row refers to only one channel grid, followed by two, three, and four-channel grids.

Pixel scale local distribution maps check the local trend of generated realizations by calculating the average and variance pooled over the calculated realizations by-pixel. The nonstationarity reproduction can be checked by comparing the local facies proportions distribution maps in regions of the model extents between the training image and the calculated realizations. The region is the subset of the image pixels that correspond to an area of interest.

Multiscale local distributions check the reproduction of the local spatial nonstationarity, i.e., the trend reproduction. We first calculate the dispersion variance of the pixels within an intermediate scale represented by a moving window, as the average of variances of all moving windows and stride (step size of the moving window) of 1. Then we summarize the relationship between the dispersion variance and scale, by varying the window size, by plotting the dispersion variance vs. window size. The facies proportion within the moving window checks the local, multiscale trend reproduction of spatial distributions and patterns [33]. The window size should be sufficient intermediate scale to ensure a reasonable trend check. We calculate facies proportions within the moving window and plot scatter maps of the proportion values vs. the TI facies proportion with the same moving windows for comparison.

Model checking with reduced dimensionality via self-attention provides a flexible comparison of generated realizations and their corresponding TIs, based on a similar procedure to [46] for dimensionality reduction, condensing the generated realizations to two dimensions. The approach uses the self-distillation with no labels method, DINO [47], with the "self-supervised" paradigm that eliminates the need for labeled data by generating its own training signals. The DINO method produces self-supervised features, which are latent features representing the most important semantic information (i.e., meaning or content) of the data learned within this paradigm. The self-supervised features distinguish among different data, facilitating clustering images with similar characteristics. The procedure begins by obtaining the self-attention features of each image using a pre-trained DINO model from [47], and then reduces the dimensionality based on the informative principal components (IPC) and t-distributed stochastic neighbor embedding (t-SNE).

4. Results and Discussions

To demonstrate our proposed workflow for SinGAN-generated model checking, we train a SinGAN with four distinct channel training images: cyclic channel model (TI1), weak trend channel model (moderate nonstationarity) (TI2), stationary channel model (TI3), and strong trend channel model (strong nonstationarity) (TI4). Our designed SinGAN model has 6 scales with a scale factor of 0.75. There are 500 iterations at each scale. We set the learning rate to be 0.0005 and α to be 10 in Equation 3. The four TIs are from the library of training images for fluvial and deepwater reservoirs [39, 48]. Figure 4 shows the four channel models, the experimental semivariograms in their major and minor directions, and the histograms. The channel models have the same dimension of 128 x 128 pixels, where 1 represents a channel and 0 represents mud. Once the SinGAN model is trained, we generate 1000 channel model realizations for each TI for the following minimum criteria checks. We randomly choose four generated realization examples for each training image case for illustration in Figure 5. We observe the possibility that the SinGAN realizations are prone to exact reproduction at the edges or corners of the image and show more variations in the central part of the channel model (such as the dead ends in TI1, R1, R3, and R4).

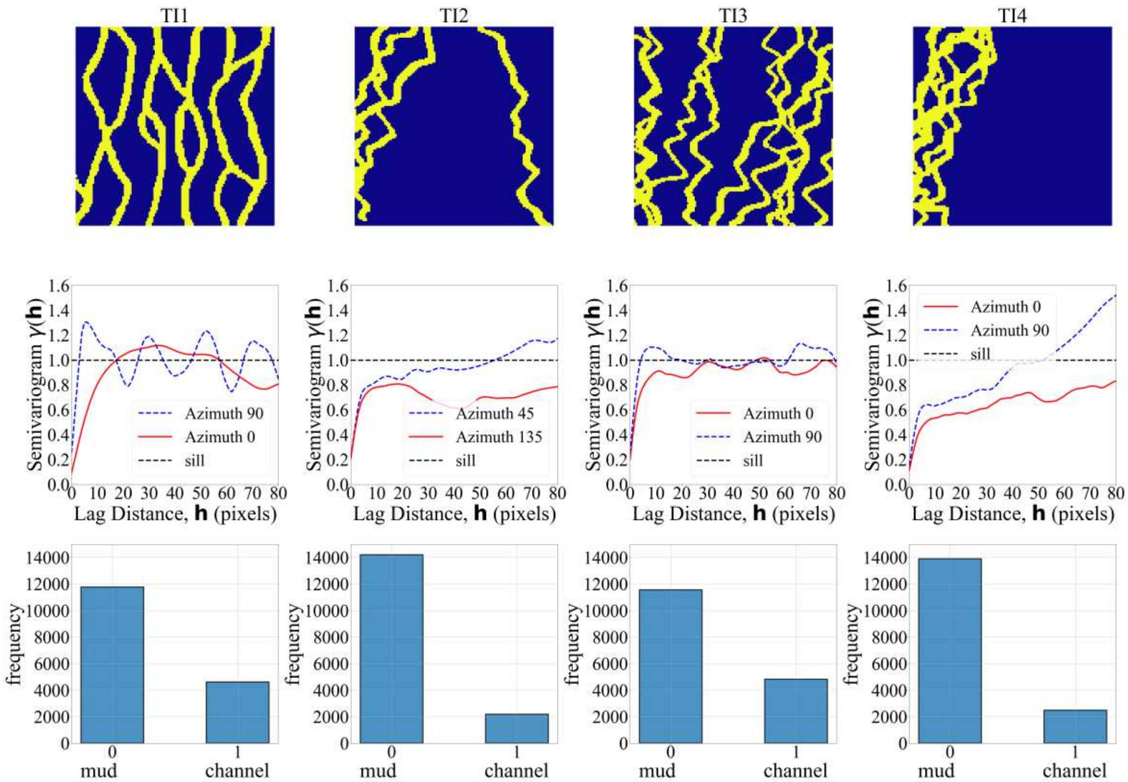

Figure 4. The first row shows four channel-model training images (TI1, TI2, TI3, and TI4) where the channel is yellow and the overbank is blue. The following rows are the experimental semivariograms in major (red line) and minor (blue dashed line) directions and histograms.

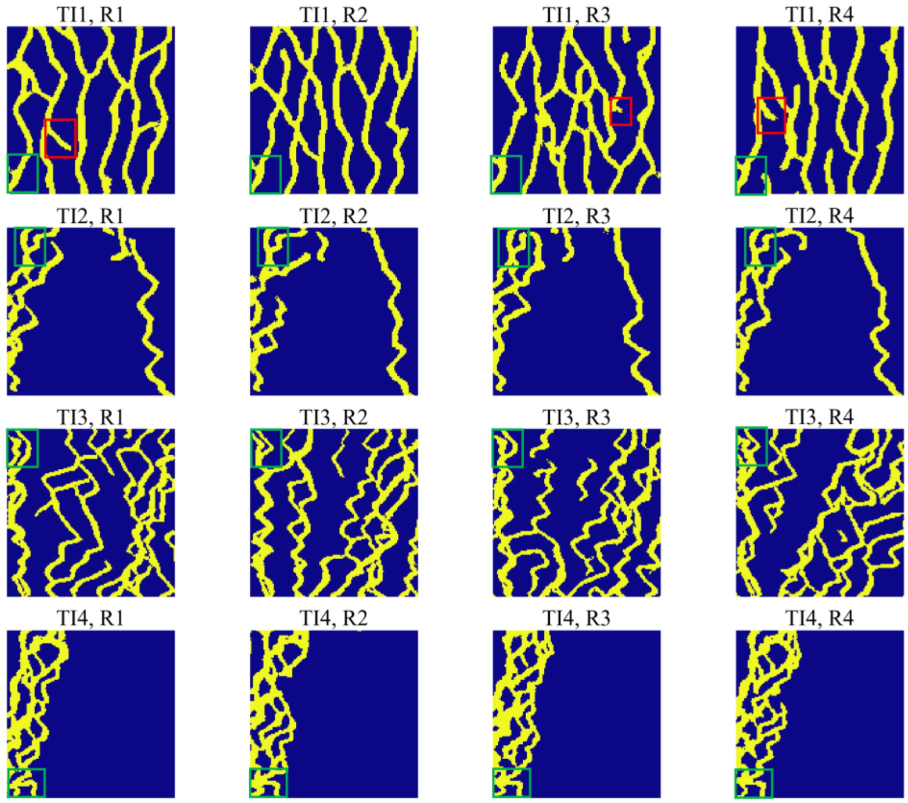

Figure 5. Four generated realization examples (R1, R2, R3, R4) for each training image case (TI1, TI2, TI3, and TI4). The green boxes depict the highly reproduced channels, and the red boxes highlight the variations.

We compare the major and minor directional experimental indicator semivariograms of the generated realizations to the training images. Figure 6 displays the major and minor azimuth semivariograms of generated realizations for each training image case and the semivariograms of the training images. The similar major and minor semivariograms indicate that the spatial structures informed by the two-point indicator semivariogram of generated realizations resemble those of the training images. The by-lag experimental semivariogram confidence interval (CI) (P25-P75) shows that the SinGAN reproduces more spread channels of TI1 and shows larger variability compared to the other TIs where their CIs cover most of the semivariograms of corresponding generated realizations.

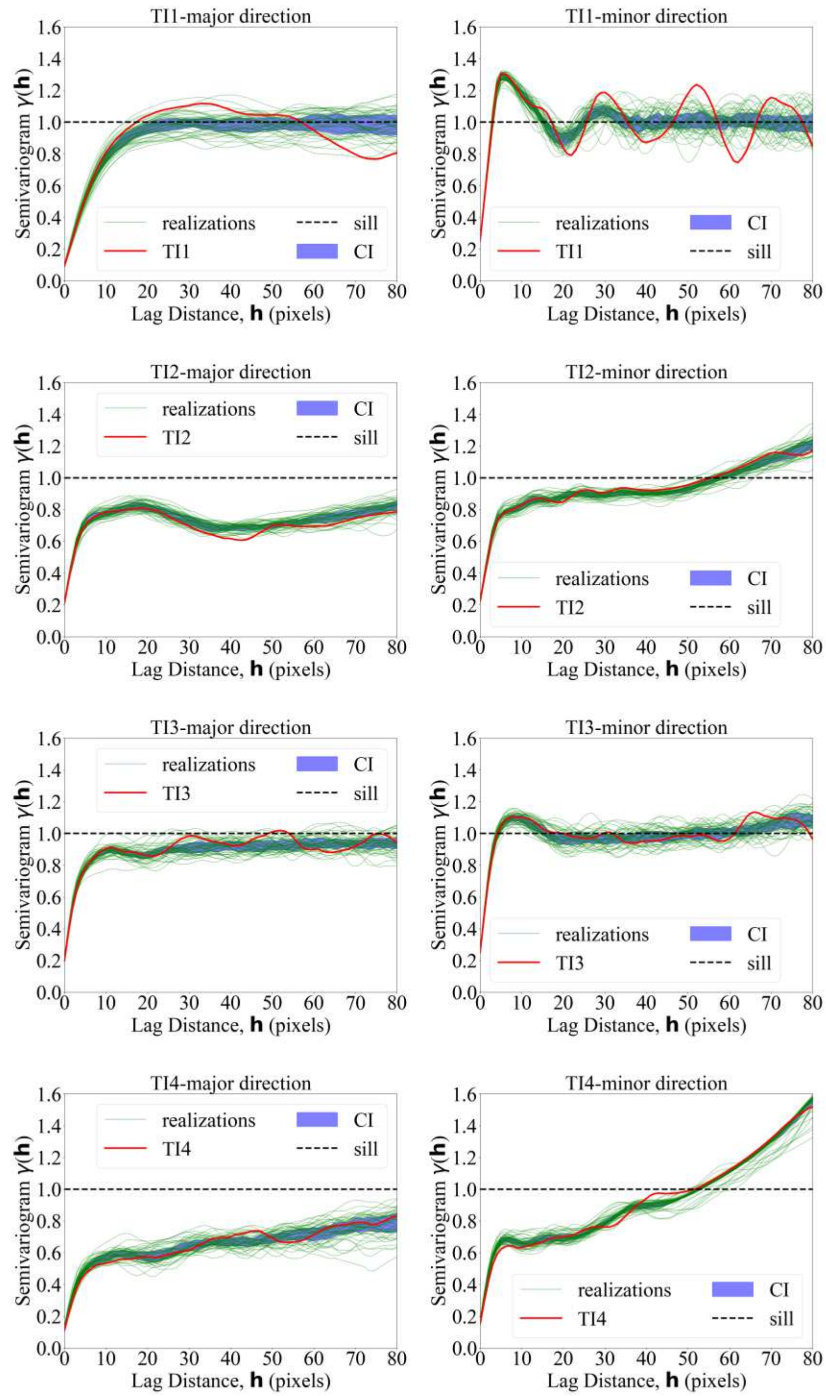

Figure 6. Major and minor experimental semivariograms (left and right columns, respectively) of generated realizations and TI1, TI2, TI3, and TI4 (from above to below). The TIs are in red and generated realizations are in green. The blue shade region depicts the by-lag experimental semivariogram confidence interval (CI): P25-P75.

We calculate the channel proportion histograms of generated realizations and compare them with their corresponding proportions from the TIs in Figure 7. The channel proportions overall are close to the channel proportion of the training image, specifically for TI1 and TI2. The channel proportions for the TI3 case span from 0.279 to 0.301, within a 5% variance of the channel proportion of TI3. The channel proportions for the TI4 case range from 0.126 to 0.159, within a 17% variance of the TI4 channel proportion, which is 0.152. We suspect the realizations for TI4 depict the largest variance in channel proportion because the channels gather on the left side of the TI and have a limited area for reproducing the channel proportion while simultaneously showing variability. To check our hypothesis, we further calculate the channel proportions within the moving window and more related analyses are provided below.

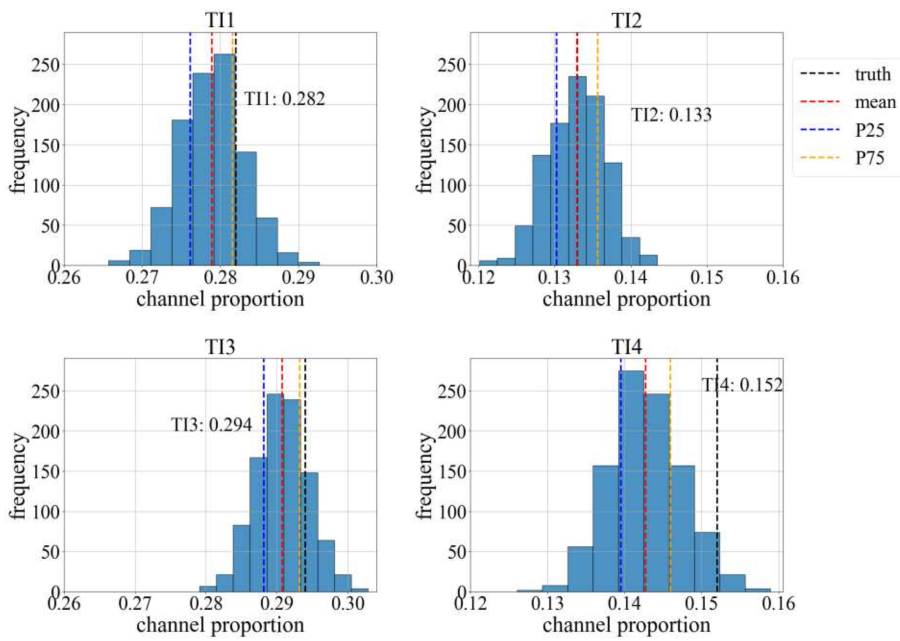

Figure 7. The histograms of channel proportions of generated realizations for each training image case with the training image channel proportion shown as a black dashed line. The mean, P25, and P75 of channel proportion distributions of generated realizations are labeled by the red, blue, and orange dashed lines, respectively.

We check the relative frequency of a specific 5-point multiple-point pattern in the generated realizations and compare them with the TI to check the multiple-point statistics reproduction. We choose a 5-point pattern for easier visualization as more point patterns are difficult to visualize, i.e., a 9-point pattern results in 510 different patterns, considering both channel and mud exist. Figure 8 shows that the relative frequency of the 5-point pattern closely resembles that of the TI with overall average relative frequencies of 0.005%, 0.009%, 0.018%, and 0.017%, respectively, suggesting that the SinGAN model captures and reproduces the spatial patterns and structure from each training image. Although there are differences in spatial continuity, stationarity, or trends among the four training images, they exhibit a shared spatial structure, as shown by the relative frequency of the 5-point histogram. For example, in cases where patterns have a relative frequency smaller than 0.005, all TIs and realizations depict similar frequencies. The observation suggests that the SinGAN can capture the fluvial and deepwater reservoir multiple-point spatial structure.

Figure 9 shows the pixel scale local distribution maps calculated over all realizations for each TI case. Given, the binary nature of the models, 1 for channel and 0 for overbank, this map communicates the proportion of realizations with channel at each pixel in the model. The local average map shows that the channel features are prone to be exactly reproduced in the corners or edges of the image (very high and very low local proportion of channels over all the realizations). The local dispersion map reveals that the variety of channel reproduction is mainly located in the center of the image, as discussed in Figure 5. We suspect this exact reproduction phenomenon is due to the SinGAN pyramid architecture, which learns a broader structure (focus more on edges or corners) at the coarse scale and adds details at the fine scale. This increasing dimension with a finer scale means smaller effective patches during training while enhancing pattern reproduction [49]. For example, Figure 10 demonstrates the feature maps from the last layer of the generator at each scale of a randomly generated realization. As the coarsest scale learns the corner channels, this information is contained in the following scales. More channel details are added gradually in scales 3, 4, and 5.

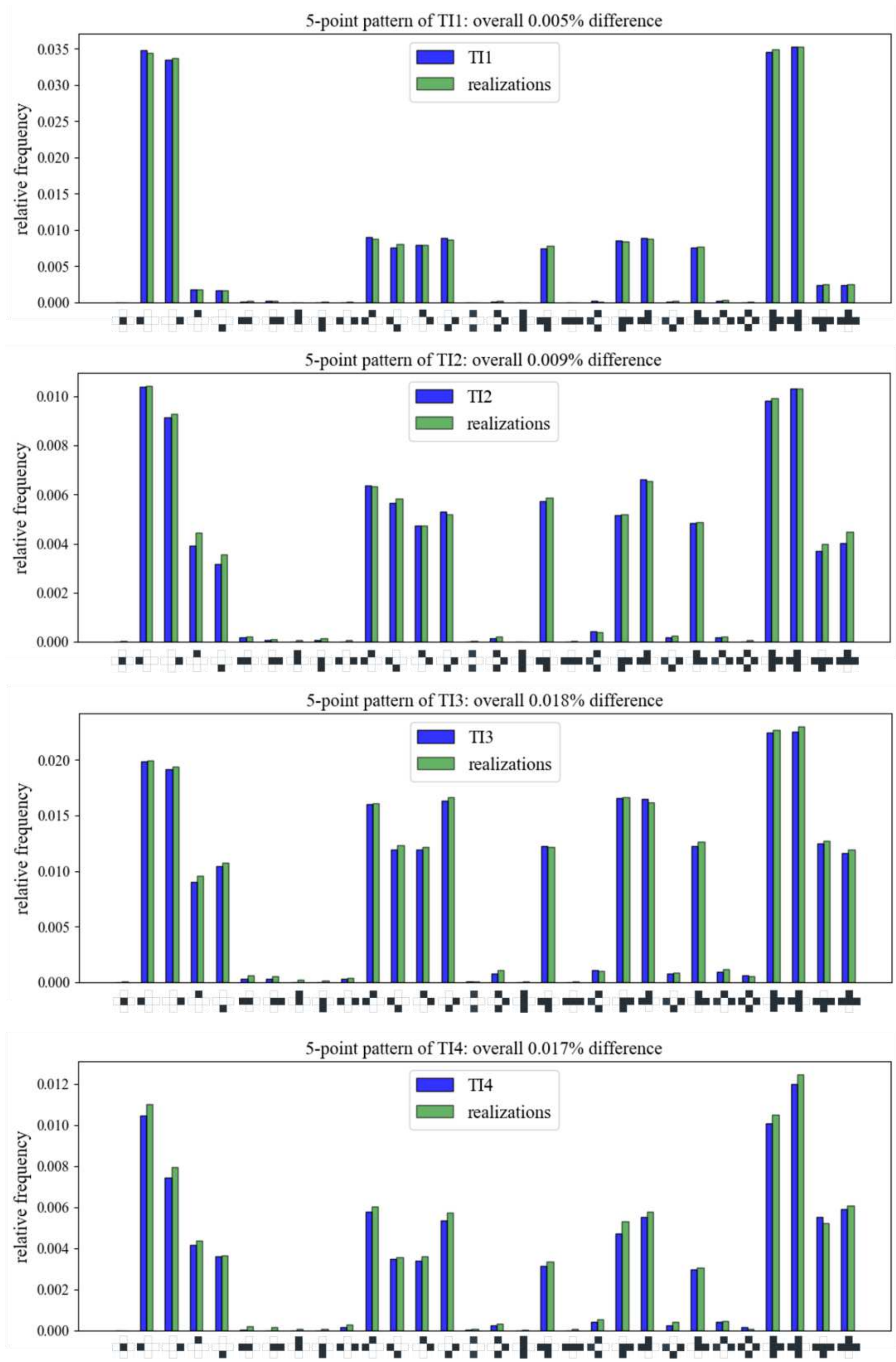

Figure 8. Five-point histogram (relative frequency) of generated realizations for each TI case (TI1, TI2, TI3, and TI4 from above to below).

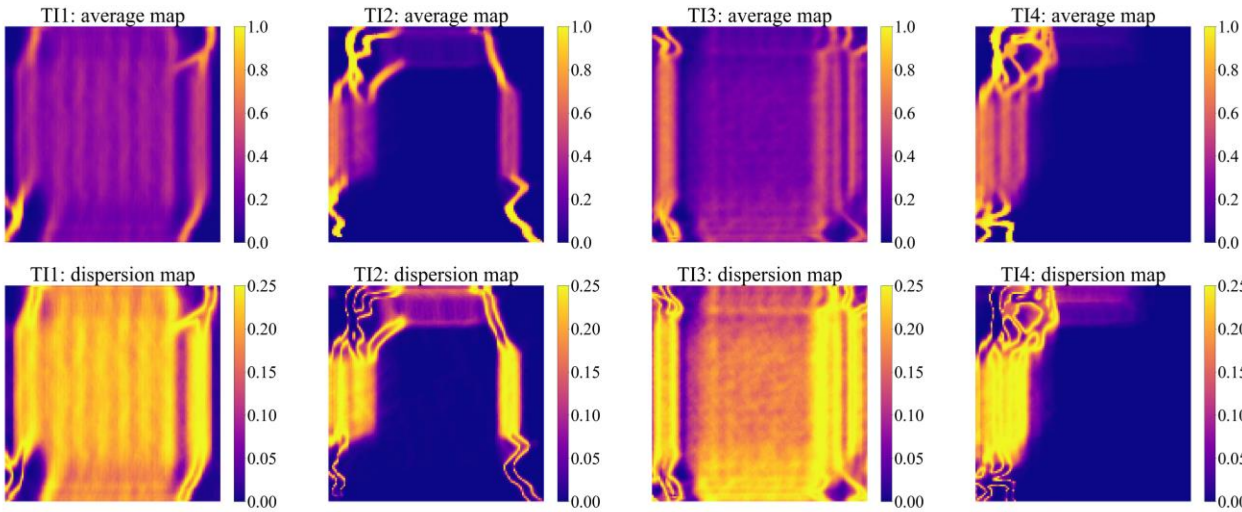

Figure 9. Local average and dispersion maps (upper and lower rows) of generated realizations for each case (TI1, TI2, TI3, and TI4 from left to right).

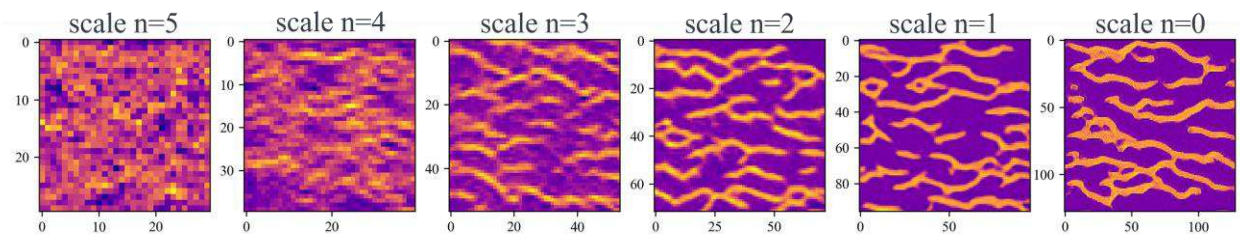

Figure 10. Feature maps of the last layer for each SinGAN scale for a randomly generated realization of the TI1 case.

The multiscale local distribution plot is the dispersion variance vs. scale function calculated with variable-size moving windows. The dispersion variance vs. scale functions are similar to the four training images in Figure 11. This function decreases to a plateau faster in TI1 and TI3 than in TI2 and TI4. Meanwhile, the dispersion variance function is more stable in TI1 and TI2 as the green curve spans are narrower than those of TI3 and TI4 in the smaller (zoom-in) window. We do not observe any inflection points among the green curves, indicating the absence of specific scales of channel clustering in generated realizations.

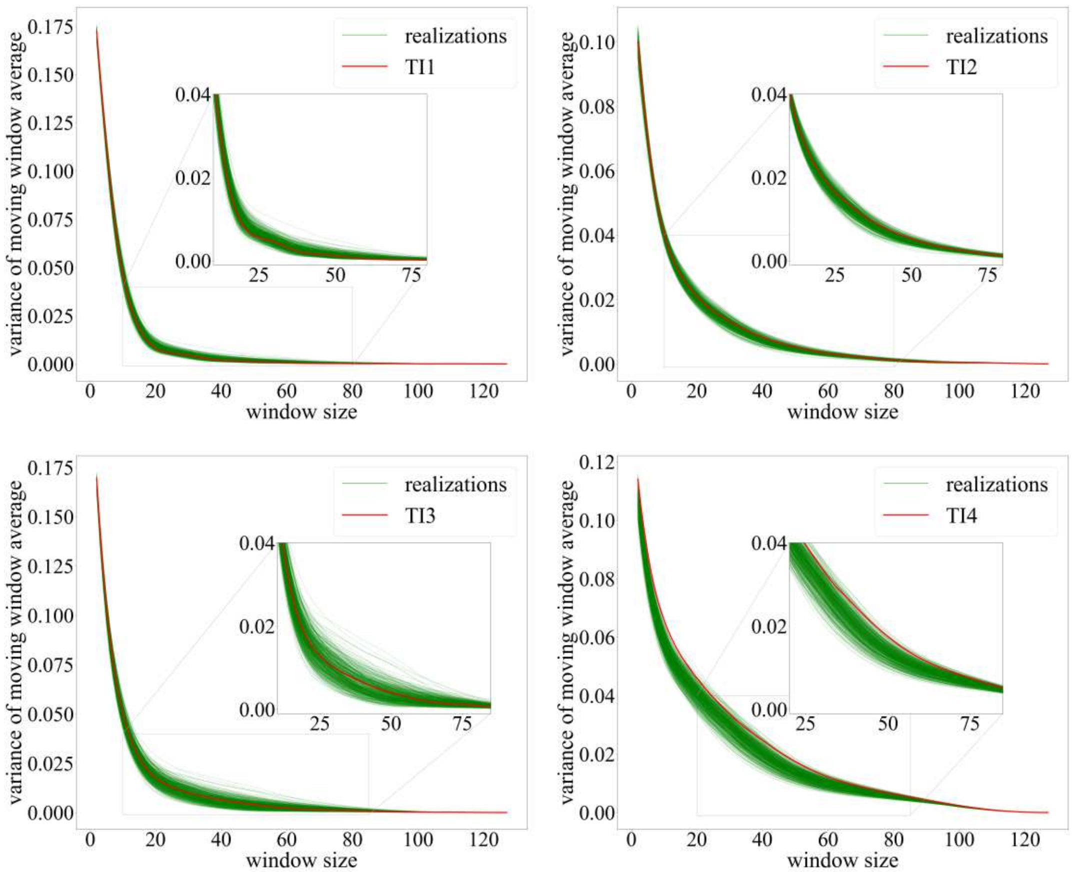

Figure 11. Dispersion variance vs. scale functions of realizations and their corresponding training images colored in red.

Figure 12 shows the channel proportions within a moving window with a stride of 1. We choose a window size of 110 for a demonstration (supported by the moving window variance reaching a plateau at the window size of 110 in Figure 11) and compare the channel proportions with that of the training image. Overall, the moving window channel proportions follow the 45-degree line. The TI4 case shows slightly less channel reproduction than other cases, as most moving window proportions fall under the 45-degree line, and the gap between the CI and truth line is bigger with increasing channel proportions.

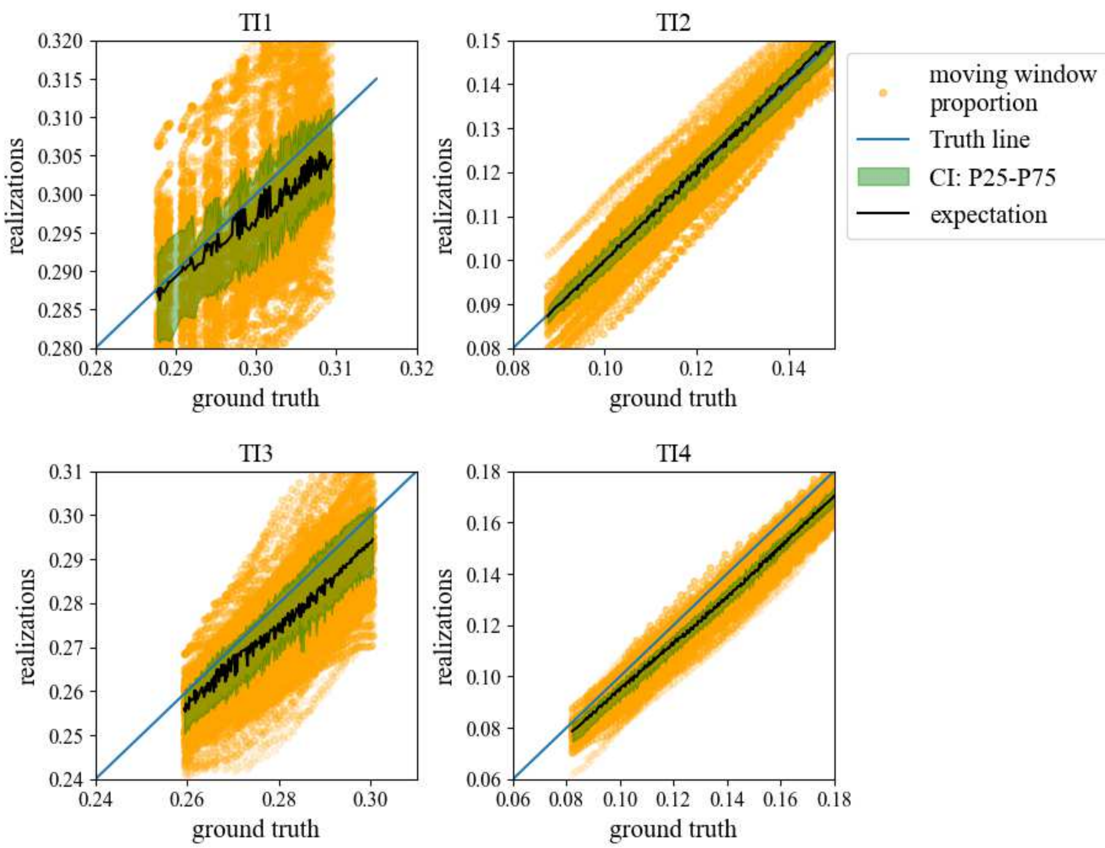

Figure 12. Channel proportions within the moving window of size 110 of each TI case. The 45-degree line is in blue, the green shaded area refers to the CI: P25-P75 and the expectation line is in black.

As observed in Figure 7 TI4 channel proportion reproduction is less than other TI cases, we rescale the channel proportion histogram distribution of TI4 to be centered at the TI global proportion, 0.152, and then check the new moving window proportions (Figure 13). Compared to the original moving window channel proportions in Figure 12, the new proportions scatter plot shows that the new CI aligns better with the 45-degree line without larger gaps in the higher channel proportions.

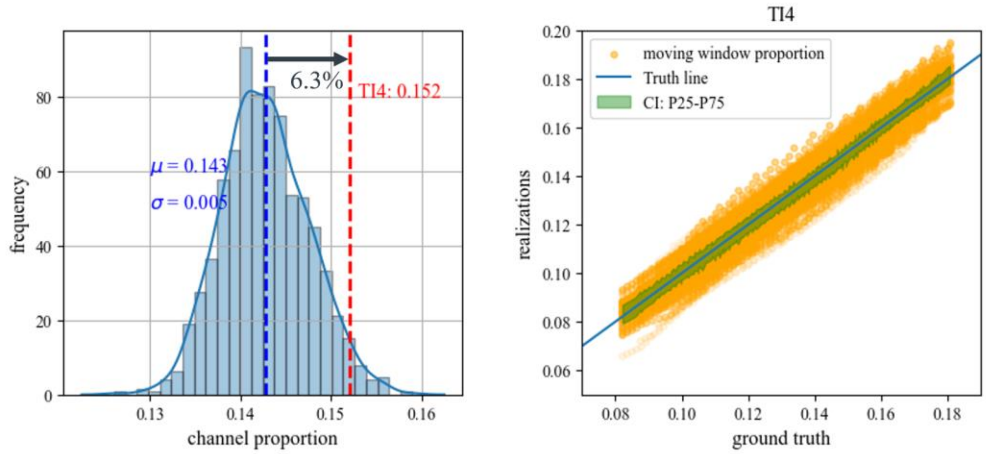

Figure 13. Channel proportion histogram of TI4, showing a 6.3% shift towards the TI global proportion (left). The updated channel proportions within the moving window (right).

We divide the training image into four equal vertical regions to quickly check the local channel proportions trend reproduction by region (Figure 14). We repeat this calculation on the generated realizations and plot the local facies proportions distributions, shown in Figure 15. Here, we randomly pick 200 realizations to show the result, as 1000 realizations are too dense to visualize. Figure 15 shows that facies proportions are close to that of the training image in each region, revealing that nonstationarity reproduction can be realized through the SinGAN model. We also observe the channel production in region III, where there is no channel in the TI4. On practice, this check may be applied to regions based on geological or engineering constraints.

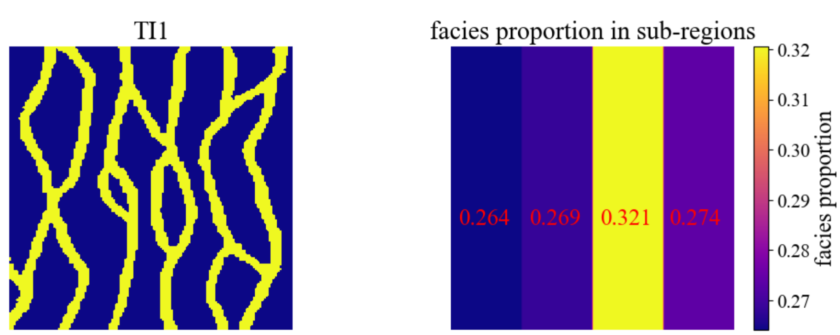

Figure 14. Facies proportion in four vertical regions (right) using TI1 (left) as an example.

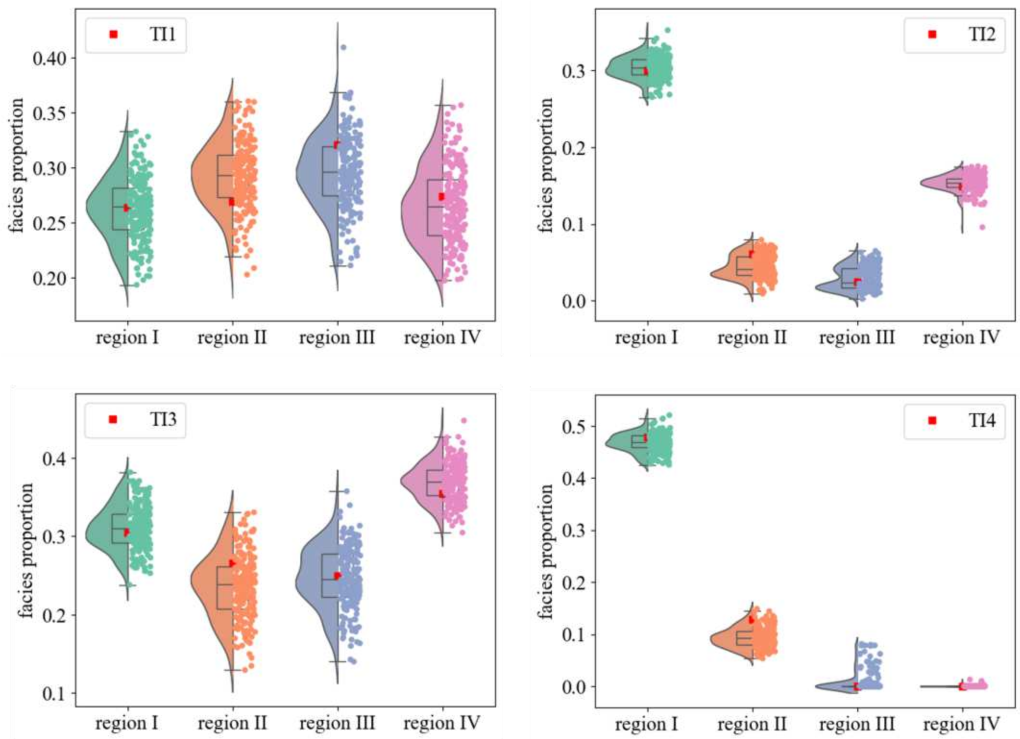

Figure 15. Facies proportion trend maps for TI1, TI2, TI3, and TI4. The 4 facies proportion distributions are for regions I, II, III, and IV, respectively. The red dot is the true facies proportion of the TI. The box displays the quartiles (Q1, median, and Q3) of the distribution while the whiskers extend to show the rest of the distribution, except for points that are determined to be outliers.

For the model checking with reduced dimensionality, we obtain the self-attention features of each image using a pre-trained DINO model, decreasing the dimension from 128x128 to 16x16 with a patch size of 8. The IPC is obtained by intersecting the explained variance from principal component analysis (PCA) and the average of 20 permutations of PCA. Finally, we further reduce the dimensionality from IPC to two using t-SNE and apply DBSCAN for clustering, as shown in Figure 16. The DBSCAN approach results in four distinct clusters representing each TI. The plot shows that DINO assigns most of the images to its corresponding TI based on their semantic information, except for five realizations of TI1 grouped in the TI3 cluster.

We hypothesize that this misclassification (a realization is assigned to a different cluster) occurs because the five generated images depict similar characteristics as TI3 (e.g., stationarity and channel proportion), making it difficult for DINO to distinguish them correctly. For example, Figure 17 demonstrates the semivariograms and facies proportions trend-maps of misclassified realizations 5, 6, and 7. We chose the previous realizations because they are closer to TI3 than other realizations (1, 2, 3, and 4) in the t-SNE space (Figure 16). Their semivariograms show a similar spatial continuity structure reproduction and the facies proportions in regions II, III, and IV, which are close to that of TI3, within 0.1 difference. Furthermore, the average and dispersion maps of TI1 and TI3 are similar in the center. Nevertheless, the misclassification is minor because they represent 0.125% of the overall generated images, suggesting the high quality of the realizations from the SinGAN method. This reduced-dimensionality analysis is conducted with unlabeled data, facilitating a more straightforward visual check of the generated realizations and the detection of misclassified realizations.

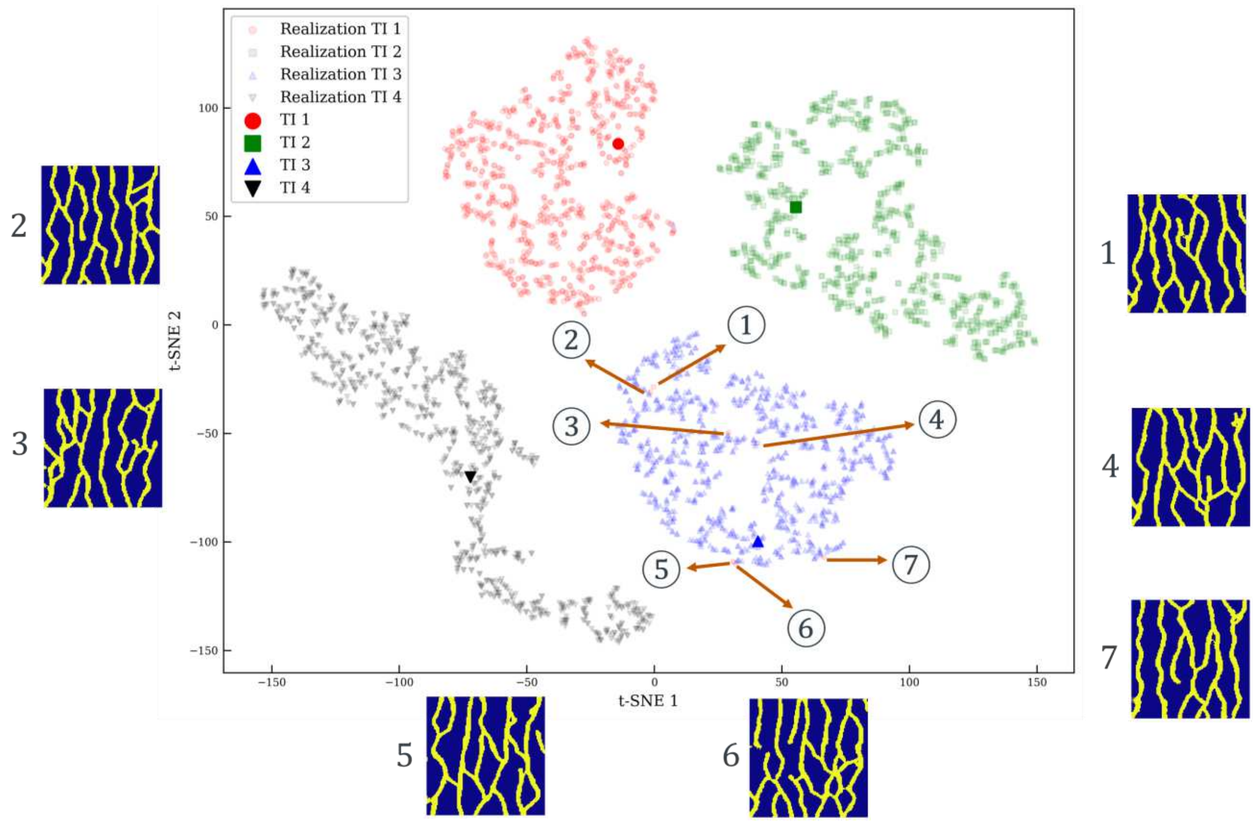

Figure 16. The visualization of generated realizations and their training images in reduced dimensional space. Realizations "1-7" belonging to the TI1 cluster are classified into the TI3 cluster.

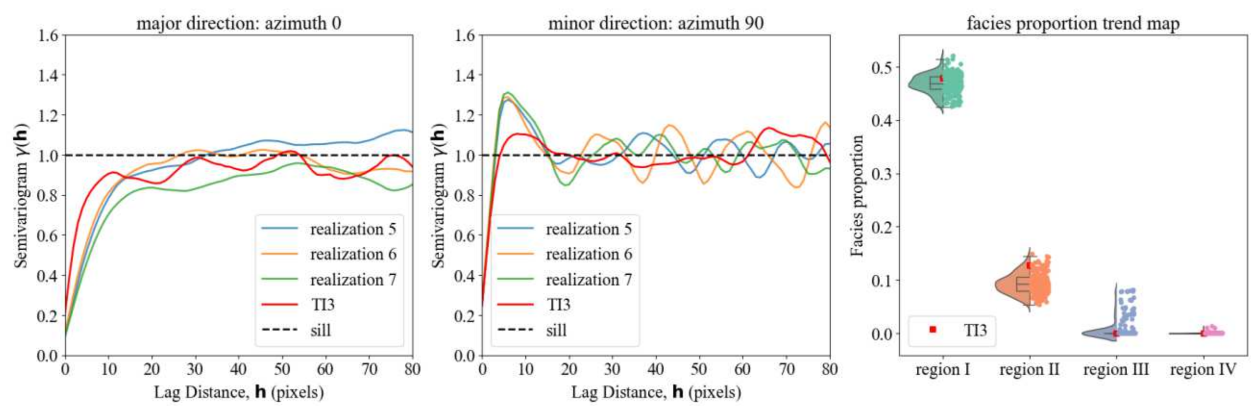

Figure 17. The model and training image experimental semivariograms in major (left) and minor (middle) directions and the facies proportions trend map (right) of misclassified realizations 5, 6, and 7.

5. Conclusions

The application of SinGAN enables the development of subsurface uncertainty models, realizations based on geological scenarios represented as single, nonstationary training images. The proposed enhanced minimum acceptance checks for enhanced model checking are tailored for quality assessment of these SinGAN-generated realizations, illustrated through distinct channelized model examples. This includes comparison between realizations and the single training image of experimental semivariograms and histograms, n-point histograms, pixel scale local distribution maps and facies proportion trend map, multiscale local distribution maps, and model dimensionality reduction analysis.

These minimum acceptance checks are demonstrated and baselined with the example of nonstationary channels and in fact show that the included metrics, spatial continuity, channel proportions, multiple-point statistics, and spatial nonstationarity can be well reproduced by SinGAN. As a limitation, we observe a slight bias in the reproduction of channel proportions in the presence of a strong spatial trend and several generated realizations depict similar characteristics to other types of TI. Additionally, given the demonstration of the new minimum acceptance criteria checks on nonstationary channel models generated by SinGAN, it is reasonable to assume that this workflow can provide guidance in other applications, such as calibrating uncertainty modeling and application to different types of subsurface models (e.g., larger scale stratigraphic and geophysical models). Future work includes improving the reproduction of complicated spatial nonstationarity by tuning the SinGAN architecture based on the proposed enhanced minimum acceptance checks.

Acknowledgments

The authors thank the Digital Reservoir Characterization Technology (DIRECT) Industry Affiliate Program at the University of Texas at Austin for supporting this work.

Statements and Declarations

The authors declare no conflicts of interest.

References

1. Ma, Y.Z., Zhang, X.: Quantitative Geosciences: Data Analytics, Geostatistics, Reservoir Characterization and Modeling. Springer International Publishing (2019)
2. Aliyari, H., Kholghi, M., Zahedi, S., Momeni, M.: Providing decision support system in groundwater resources management for the purpose of sustainable development. J. Water Supply Res. Technol.-Aqua. 67, 423–437 (2018). https://doi.org/10.2166/aqua.2018.130
3. Linde, N., Renard, P., Mukerji, T., Caers, J.: Geological realism in hydrogeological and geophysical inverse modeling: A review. Adv. Water Resour. 86, 86–101 (2015). https://doi.org/10.1016/j.advwatres.2015.09.019
4. Strebelle, S.: Multiple-Point Statistics Simulation Models: Pretty Pictures or Decision-Making Tools? Math. Geosci. 53, 267–278 (2021). https://doi.org/10.1007/s11004-020-09908-8
5. Hu, L.Y., Chugunova, T.: Multiple-point geostatistics for modeling subsurface heterogeneity: A comprehensive review. Water Resour. Res. 44, (2008). https://doi.org/10.1029/2008WR006993

6. Feng, R., Grana, D., Mukerji, T., Mosegaard, K.: Application of Bayesian Generative Adversarial Networks to Geological Facies Modeling. Math. Geosci. 54, 831–855 (2022). https://doi.org/10.1007/s11004-022-09994-w
7. Pyrcz, M., Deutsch, C.V.: Geostatistical reservoir modeling. New York, New York: Oxford University Press, Oxford (2014)
8. Chen, Q., Liu, G., Ma, X., Li, X., He, Z.: 3D stochastic modeling framework for Quaternary sediments using multiple-point statistics: A case study in Minjiang Estuary area, southeast China. Comput. Geosci. 136, 104404 (2020). https://doi.org/10.1016/j.cageo.2019.104404
9. Okabe, H., Blunt, M.J.: Pore space reconstruction using multiple-point statistics. J. Pet. Sci. Eng. 46, 121–137 (2005). https://doi.org/10.1016/j.petrol.2004.08.002
10. Journel, A.G.: Nonparametric estimation of spatial distributions. J. Int. Assoc. Math. Geol. 15, 445–468 (1983). https://doi.org/10.1007/BF01031292
11. Journel, A.G., Isaaks, E.H.: Conditional Indicator Simulation: Application to a Saskatchewan uranium deposit. J. Int. Assoc. Math. Geol. 16, 685–718 (1984). https://doi.org/10.1007/BF01033030
12. Matheron, G., Beucher, H., de Fouquet, C., Galli, A., Guerillot, D., Ravenne, C.: Conditional Simulation of the Geometry of Fluvio-Deltaic Reservoirs. Presented at the SPE Annual Technical Conference and Exhibition September 27 (1987)
13. de Vries, L.M., Carrera, J., Falivene, O., Gratacós, O., Slooten, L.J.: Application of Multiple Point Geostatistics to Non-stationary Images. Math. Geosci. 41, 29–42 (2009). https://doi.org/10.1007/s11004-008-9188-y
14. Guardiano, F.B., Srivastava, R.M.: Multivariate Geostatistics: Beyond Bivariate Moments. In: Soares, A. (ed.) Geostatistics Tróia ’92. pp. 133–144. Springer Netherlands, Dordrecht (1993)

15. Avalos, S., Ortiz, J.M.: Recursive convolutional neural networks in a multiple-point statistics framework. Comput. Geosci. 141, 104522 (2020). https://doi.org/10.1016/j.cageo.2020.104522
16. Strebelle, S.: Conditional Simulation of Complex Geological Structures Using Multiple-Point Statistics. Math. Geol. 34, 1–21 (2002). https://doi.org/10.1023/A:1014009426274
17. Zhang, T., Switzer, P., Journel, A.: Filter-Based Classification of Training Image Patterns for Spatial Simulation. Math. Geol. 38, 63–80 (2006). https://doi.org/10.1007/s11004-005-9004-x
18. Azevedo, L., Paneiro, G., Santos, A., Soares, A.: Generative adversarial network as a stochastic subsurface model reconstruction. Comput. Geosci. 24, 1673–1692 (2020). https://doi.org/10.1007/s10596-020-09978-x
19. Deutsch, C.: ANNEALING TECHNIQUES APPLIED TO RESERVOIR MODELING AND THE INTEGRATION OF GEOLOGICAL AND ENGINEERING (WELL TEST) DATA. Presented at the (1992)
20. Zuo, C., Pan, Z., Yin, Z., Guo, C.: A nearest neighbor multiple-point statistics method for fast geological modeling. Comput. Geosci. 167, 105208 (2022). https://doi.org/10.1016/j.cageo.2022.105208
21. Mahmud, K., Mariethoz, G., Caers, J., Tahmasebi, P., Baker, A.: Simulation of Earth textures by conditional image quilting. Water Resour. Res. 50, 3088–3107 (2014). https://doi.org/10.1002/2013WR015069
22. Caers, J., Journel, A.G.: Stochastic Reservoir Simulation Using Neural Networks Trained on Outcrop Data. Presented at the SPE Annual Technical Conference and Exhibition September 27 (1998)
23. Liu, Y., Zhang, X., Guo, W., Kang, L., Gao, J., Yu, R., Sun, Y., Pan, M.: Research Status of and Trends in 3D Geological Property Modeling Methods: A Review. Appl. Sci. 12, 5648 (2022). https://doi.org/10.3390/app12115648

24. Goodfellow, I.J., Pouget-Abadie, J., Mirza, M., Xu, B., Warde-Farley, D., Ozair, S., Courville, A., Bengio, Y.: Generative Adversarial Networks. ArXiv14062661 Cs Stat. (2014)
25. Mosser, L., Dubrule, O., Blunt, M.J.: Reconstruction of three-dimensional porous media using generative adversarial neural networks. Phys. Rev. E. 96, 043309 (2017). https://doi.org/10.1103/PhysRevE.96.043309
26. Li, Z., Meier, M.-A., Hauksson, E., Zhan, Z., Andrews, J.: Machine Learning Seismic Wave Discrimination: Application to Earthquake Early Warning. Geophys. Res. Lett. 45, 4773–4779 (2018). https://doi.org/10.1029/2018GL077870
27. Hu, F., Wu, C., Shang, J., Yan, Y., Wang, L., Zhang, H.: Multi-condition controlled sedimentary facies modeling based on generative adversarial network. Comput. Geosci. 171, 105290 (2023). https://doi.org/10.1016/j.cageo.2022.105290
28. Jo, H., Santos, J.E., Pyrcz, M.J.: Conditioning well data to rule-based lobe model by machine learning with a generative adversarial network. Energy Explor. Exploit. 38, 2558–2578 (2020). https://doi.org/10.1177/0144598720937524
29. Song, S., Mukerji, T., Hou, J.: Geological Facies modeling based on progressive growing of generative adversarial networks (GANs). Comput. Geosci. 25, 1251–1273 (2021). https://doi.org/10.1007/s10596-021-10059-w
30. Zhang, T., Ji, X., Zhang, A.: Reconstruction of fluvial reservoirs using multiple-stage concurrent generative adversarial networks. Comput. Geosci. 25, 1983–2004 (2021). https://doi.org/10.1007/s10596-021-10086-7
31. Shaham, T.R., Dekel, T., Michaeli, T.: SinGAN: Learning a Generative Model from a Single Natural Image, http://arxiv.org/abs/1905.01164, (2019)

32. Leuangthong, O., McLennan, J.A., Deutsch, C.V.: Minimum Acceptance Criteria for Geostatistical Realizations. Nat. Resour. Res. 13, 131–141 (2004). https://doi.org/10.1023/B:NARR.0000046916.91703.bb
33. Boisvert, J.B., Pyrcz, M.J., Deutsch, C.V.: Multiple Point Metrics to Assess Categorical Variable Models. Nat. Resour. Res. 19, 165–175 (2010). https://doi.org/10.1007/s11053-010-9120-2
34. Strébelle, S.: Sequential simulation drawing structures from training images, (2000)
35. Hansen, T.M., Vu, L.T., Mosegaard, K., Cordua, K.S.: Multiple point statistical simulation using uncertain (soft) conditional data. Comput. Geosci. 114, 1–10 (2018). https://doi.org/10.1016/j.cageo.2018.01.017
36. Yang, Z., Chen, Q., Cui, Z., Liu, G., Dong, S., Tian, Y.: Automatic reconstruction method of 3D geological models based on deep convolutional generative adversarial networks. Comput. Geosci. 26, 1135–1150 (2022). https://doi.org/10.1007/s10596-022-10152-8
37. Pan, W., Chen, J., Mohamed, S., Jo, H., Santos, J.E., Pyrcz, M.J.: Efficient Subsurface Modeling with Sequential Patch Generative Adversarial Neural Networks. Presented at the SPE Annual Technical Conference and Exhibition October 9 (2023)
38. Laloy, E., Hérault, R., Jacques, D., Linde, N.: Training-Image Based Geostatistical Inversion Using a Spatial Generative Adversarial Neural Network. Water Resour. Res. 54, 381–406 (2018). https://doi.org/10.1002/2017WR022148
39. Strebelle, S., Zhang, T.: Non-stationary multiple-point geostatistical models. Geostat. Banff 2004. 235–244 (2005)

40. Gulrajani, I., Ahmed, F., Arjovsky, M., Dumoulin, V., Courville, A.C.: Improved Training of Wasserstein GANs. In: Advances in Neural Information Processing Systems. Curran Associates, Inc. (2017)
41. Chen, M., Wu, S., Bedle, H., Xie, P., Zhang, J., Wang, Y.: Modeling of subsurface sedimentary facies using Self-Attention Generative Adversarial Networks (SAGANs). J. Pet. Sci. Eng. 214, 110470 (2022). https://doi.org/10.1016/j.petrol.2022.110470
42. Wu, B.M., Subbarao, K.V., Ferrandino, F.J., Hao, J.J.: Spatial Analysis Based on Variance of Moving Window Averages. J. Phytopathol. 154, 349–360 (2006). https://doi.org/10.1111/j.1439-0434.2006.01105.x
43. Liu, L., Prodanović, M., Pyrcz, M.J.: Impact of geostatistical nonstationarity on convolutional neural network predictions. Comput. Geosci. (2022). https://doi.org/10.1007/s10596-022-10181-3
44. Liu, L., Santos, J.E., Prodanović, M., Pyrcz, M.J.: Mitigation of spatial nonstationarity with vision transformers. Comput. Geosci. 178, 105412 (2023). https://doi.org/10.1016/j.cageo.2023.105412
45. Boisvert, J.B., Pyrcz, M.J., Deutsch, C.V.: Multiple-Point Statistics for Training Image Selection. Nat. Resour. Res. 16, 313–321 (2007). https://doi.org/10.1007/s11053-008-9058-9
46. Salazar, J.J., Maldonado-Cruz, E., Ochoa, J., Pyrcz, M.J.: Self-Supervised Learning for Seismic Data: Enhancing Model Interpretability with Seismic Attributes. IEEE Trans. Geosci. Remote Sens. (2023)
47. Caron, M., Touvron, H., Misra, I., Jegou, H., Mairal, J., Bojanowski, P., Joulin, A.: Emerging Properties in Self-Supervised Vision Transformers. In: 2021 IEEE/CVF International Conference on Computer Vision (ICCV). pp. 9630–9640. IEEE, Montreal, QC, Canada (2021)

48. Pyrcz, M.J., Boisvert, J.B., Deutsch, C.V.: A library of training images for fluvial and deepwater reservoirs and associated code. Comput. Geosci. 34, 542–560 (2008). https://doi.org/10.1016/j.cageo.2007.05.015
49. Mariethoz, P.G., Caers, J.: Multiple-point Geostatistics: Stochastic Modeling with Training Images. John Wiley & Sons (2014)